International Journal of Pharmaceutics: X 6 (2023) 100213

Contents lists available at ScienceDirect

International Journal of Pharmaceutics: X

journal homepage: www.sciencedirect.com/journal/international-journal-of-pharmaceutics-x

Polymeric nanocomposite hydrogel scaffold for jawbone regeneration: The role of rosuvastatin calcium-loaded silica nanoparticles

Islam M. Adel [a,*], Mohamed F. ElMeligy [a], Mohammed S. Amer [b], Nermeen A. Elkasabgy [a]

[a] Department of Pharmaceutics and Industrial Pharmacy, Faculty of Pharmacy, Cairo University, Kasr El-Aini Street, Cairo 11562, Egypt
[b] Department of Surgery, Anaesthesiology and Radiology, Faculty of Veterinary Medicine, Cairo University, Cairo 12211, Egypt

ARTICLE INFO

Keywords:
Rosuvastatin
Silica nanoparticles
Sodium alginate
Hydrogel scaffolds
Jawbone
Tissue engineering

ABSTRACT

Bones are subject to different types of damages ranging from simple fatigue to profound defects. In serious cases, the endogenous healing mechanism is not capable of healing the damage or restoring the normal structure and function of the bony tissue. **The aim** of this research was to achieve a sustained delivery of rosuvastatin and assess its efficacy in healing bone tissue damage. Rosuvastatin was entrapped into silica nanoparticles and the system was loaded into an alginate hydrogel to be implanted in the damaged tissue. Silica nanoparticles were formulated based on a modified Stöber technique and alginate hydrogel was prepared via sprinkling alginate onto silica nanoparticle dispersion followed by addition of $CaCl_2$ to promote crosslinking and hydrogel rigidification. The selected nanoparticle formulation possessed high % drug content (100.22±0.67%), the smallest particle size (221.00±7.30 nm) and a sustained drug release up to 4 weeks (98.72±0.52%). The fabricated hydrogel exhibited a further delay in drug release (81.52±4.81% after 4 weeks). FT-IR indicated the silica nanoparticle formation and hydrogel crosslinking. SEM visualized the porous and dense surface of hydrogel. In-vivo testing on induced bone defects in New Zealand rabbits revealed the enhanced rate of new bone tissue formation, its homogeneity in color as well as similarity in structure to the original tissue.

1. Introduction

Not just that the bone tissue plays a very crucial role in organ and entire body movements, but also it serves several other essential functions. For instance, it hosts bone marrow and is also leading a protective role towards many body organs. Bone tissue is involved in the regulation of normal endocrine function as well as supporting muscles (Battafarano et al., 2021). Bone is subject to tissue damage ranging from simple fatigue to deep tissue damage. For simple tissue damage, usually the bone's tissue repair mechanism is sufficient to counteract the damage. However, in more serious circumstances, different interventions are required, of which, bone grafts remain the gold standard (Brydone et al., 2010). Grafting exposes the subject to several risks including the likes of graft rejection, limited donor compatibility, risk of infection and high patient morbidity. To overcome the shortcomings of grafting, the multidisciplinary science of tissue engineering (TE) had emerged. To put it into short words, TE aims at creating a solid matrix, a scaffold, that perfectly fits into the defect and enhances tissue regeneration. Not only that, but the implanted scaffold can accommodate biological or chemical agents, cells, and growth factors to further fasten the rate of healing (Adel et al., 2022). Hydrogels are scaffolds that closely resemble extracellular matrix (ECM) which render them favorable in TE. Being hydrophilic, hydrogels tend to swell in aqueous environment and facilitate nutrients and O_2 exchange. They can be used in TE to act as support matrices for the new tissues, drug carriers as well as acceleration wound healing and positive effect on blood vessels formation (Adel et al., 2022). Alginate (AL) is a natural biopolymer used in scaffold fabrication with long history in bone tissue engineering. That is mainly owing to several characteristics like excellent biocompatibility, biodegradability, non-toxicity, and optimum gelling ability in presence of divalent cations such as Ca^{2+} (Sahoo and Biswal, 2021). When it comes to bone tissue engineering, AL was found to stimulate osteogenic differentiation and exert positive effects over osteocalcin, alkaline phosphatase levels, cellular viability and proliferation (Florczyk et al., 2012; Rubert et al., 2012; Venkatesan et al., 2015).

Nanoparticles (NPs) have been long associated with drug delivery attributed to small particle size, large surface area as well as enhanced drug solubility and cellular uptake. NPs can be categorized based on their nature into organic nanoparticles (polymer-based or lipid-based) and inorganic nanoparticles (like silica nanoparticles, SNPs). SNPs

* Corresponding author at: Faculty of Pharmacy, Cairo University, Kasr El-Aini Street, Cairo 11562, Egypt.
E-mail address: islam.hashim@pharma.cu.edu.eg (I.M. Adel).

https://doi.org/10.1016/j.ijpx.2023.100213
Received 18 August 2023; Received in revised form 13 September 2023; Accepted 30 September 2023
Available online 2 October 2023

usually range from 2 to 50 nm but can also be larger (up to 500 nm) with plenty of silanol groups (Si-OH) onto their surfaces (Selvarajan et al., 2020). SNPs were selected as the drug delivery system of choice for their evident role in bone regeneration. They are thought to exert a regulatory effect on osteoblasts differentiation and inhibitory effect over osteoclasts differentiation (Beck et al., 2011; Li et al., 2021). Other merits include biocompatibility, excellent tolerability, and minimal in-vivo side effects (Selvarajan et al., 2020). SNPs present significant improvements over traditional NPs. For instance, they have good mechanical stability which can be beneficial for TE particularly in load-bearing tissues. Large-pore SNPs (mesoporous SNPs) offer larger capacities for higher drug loading (Janjua et al., 2021). SNPs can be easily tuned in terms of pore size and volume as well as surface charge and functionality. Both aspects affect the loading, release, and clearance of the drug (Porrang et al., 2022). At the same time, they resist harsh biological conditions such as the acidic nature of the stomach (Janjua et al., 2021). Moreover, SNPs vastly improve the bioavailability of several agents either when used solely as SNPs (such as Fenofibrate-loaded SNPs) or when they are hybridized with other lipid systems (such as Simvastatin-loaded lipoceramic SNPs and Ibuprofen-loaded silica-lipid NPs) (Bukara et al., 2016; Meola et al., 2020; Tan et al., 2014). The preparation of SNPs can be achieved through several approaches, the most common of which are the bottom-up, Stöber, technique and the top-down, microemulsion, technique. Stöber's approach utilizes a silica source like tetraethyl orthosilicate (TEOS) that undergoes hydrolysis and nucleation in a water-alcohol solution in the presence of amino groups (nitrogen source) as a catalyst. Following a polycondensation step occurs with the formation of siloxane bonds (Bondareva et al., 2020; Stöber et al., 1968). However, long synthesis time and harsh conditions implied in this technique (high temperatures and presence of ammonia) are major drawbacks to this approach. On the other hand, the microemulsion approach relies on using surfactants to form micelles in either a w/o or an o/w system. Hydrolysis, polycondensation and formation of SNP occur within the formed micelles (Selvarajan et al., 2020; Arriagada and Osseo-Asare, 1995). The process is, though, expensive to use on large scale and mandates large volumes of surfactant to be used (Zaghloul et al., 2022).

Statins are medicinal compounds originally used for their cholesterol lowering profiles. Over time, they were found to exert a striking osteoinductive activity. The exact mechanism by which they function is rather combinatory of several actions as follows. Extensive in-vitro and in-vivo testing concluded that statins have a potential down-regulatory effect on osteoblasts apoptosis, promote tissue vascularization and bone mineralization (Safari et al., 2020). Rosuvastatin calcium (RSV) is a peculiar statin molecule that offers several advantages over other statins. It is a water-soluble molecule (saturation solubility 7.8 mg/mL) which makes it compatible with physiological environment and tissue exudates (Maged et al., 2018). It has fewer side effects all while maintaining its activity for longer times due to its reduced hepatic metabolism by CYP2C19 (Safari et al., 2020; Luvai et al., 2012).

The goal of this research was to assess the efficiency of a developed drug-entrapped SNPs loaded into an implantable hydrogel scaffold in providing sustained drug delivery and promoting bone tissue healing. The preparation technique was based on a modified Stöber technique that is simpler and involving less harsh conditions. The technique involved a simple crosslinking reaction between TEOS and chitosan hydrochloride (Ch) as nitrogen source and was carried at room temperature. No alkalis, acids, surfactants, or excessive temperatures were used. In order to identify the best formulation, in-vitro characterization was conducted. That included measurements of percentage drug content, particle size, polydispersity index and zeta potential as well as analysis of in-vitro release kinetics. Morphology of the selected SNP formulation was examined using TEM while inter-ingredients interactions were tested using FT-IR. The selected formulation was then loaded into AL hydrogel and both in-vitro release and FT-IR tests were repeated. DSC was conducted to evaluate the thermal behavior of the hydrogel as well as individual ingredients. Moving on, surface morphology of RSV-entrapped SNP-loaded hydrogel (AL-RSNP) was scanned using SEM. Finally, the hydrogel was sterilized by gamma irradiation and tested in vivo using New Zealand white rabbits to assess their effectiveness in healing damage of the jawbone tissue both at macroscopic and microscopic levels.

2. Materials and methodology

2.1. Materials

RSV was kindly supplied by Hikma Pharmaceuticals, Ch was procured from Zhejiang Chemicals Import and Export Corporation (Hangzhou, China), AL was brought from Fluka, Switzerland. TEOS (98%) and dialysis cellulose membrane (molecular weight cutoff 14,000 g/mol) were purchased from Sigma Aldrich, St. Louis, USA. All other chemicals and solvent used were of analytical grade.

2.2. Preparation of Rosuvastatin-loaded silica nanoparticles (RSNPs)

The preparation of RSNP was based on Stöber technique with some modifications (Zaghloul et al., 2022). An aqueous solution of Ch (0.1% *w/v*) was first prepared by dissolving Ch in distilled water under magnetic stirring (Stuart, SB162, UK) at 400 rpm and $37\pm0.2^{\circ}C$ for 5 min (aqueous phase). At the same time, an alcoholic solution of RSV in propylene glycol (PG) was prepared by vortexing (Reax Top Vortex Mixer, Heidolph, Germany) accurate amounts of RSV in a defined volume of PG for 5 min (alcoholic phase). Following, the alcoholic solution was slowly added to the aqueous solution under magnetic stirring at 400 rpm for 10 min. After complete miscibility of the two solutions, the required volume of TEOS was added dropwise to the mixed solution and the final mixture was left to stir under the same conditions overnight. The resultant dispersion was stored in sealed vials for further evaluation. Table 1 shows the composition of different RSNPs formulations prepared.

2.3. Characterization of the prepared Rosuvastatin silica nanoparticles (RSNPs)

2.3.1. Particle Size (PS), Zeta Potential (ZP), and Polydispersity Index (PDI) measurements

PS, ZP and PDI measurements for the prepared formulations were taken using Malvern ZetaSizer Nano ZS (Malvern Instruments, Worcestershire, UK). Samples were appropriately diluted in distilled water and thoroughly mixed prior to measurements.

2.3.2. Drug content (% DC)

Accurate volumes of the RSNP dispersions were measured and mixed with isopropyl alcohol to extract RSV and determine its concentrations using UV Spectrophotomer (model UV-1601 PC; Shimadzu, Kyoto, Japan) at $\lambda_{max} = 240$ nm. The % DC was calculated as follows.

$$\%DC = \frac{\text{Actual RSV content}}{\text{Theoretical RSV content}} \times 100$$

2.3.3. In-vitro release testing

The in-vitro release behavior of crude RSV from the prepared RSNPs was assayed using the dialysis bag method (Abd-Elal et al., 2023; Tawfik et al., 2023). Briefly, specific volume of each RSNPs formulations (equivalent to 1 mg RSV) was placed in a dialysis cellulose bag (previously soaked in distilled water overnight and locked from one end). The bag was locked from the other end and placed in a 90 mL glass bottle prefilled with 50 mL phosphate buffer saline (PBS; pH 7.4) as the release medium. The glass bottles were transferred to a thermostatically controlled shaker (Unimax, IKA, Germany) adjusted at 50 rpm and $37\pm0.2^{\circ}C$. At predetermined time intervals, a 3 mL sample from each glass bottle was withdrawn and analyzed for RSV content at 240 nm

Table 1
Composition and Characterization of the prepared RSV-loaded Silica Nanoparticles.

Formulation code	**, * and **Composition					Characterization			
	**Hydroalcoholic solution (v/v)		Nitrogen source (% w/v)	Silica source (% v/v)	Drug (%w/v)	PS	PDI	ZP	%DC
	Aqueous phase	Alcoholic phase	Ch. HCl	TEOS	RSV				
RSNP1	1	1	0.1	10	0.2	342.90±34.60	0.59±0.07	11.70±0.10	94.91±1.29
RSNP2	1	1	0.1	20	0.2	221.00±7.30	0.39±0.02	12.90±2.80	100.22±0.67
RSNP3	2	1	0.1	10	0.2	496.25±1.85	0.63±0.15	9.97±2.23	89.82±0.22
RSNP4	2	1	0.1	20	0.2	362.35±54.05	0.47±0.05	10.85±0.75	99.16±0.62
RSNP5	3	1	0.1	10	0.2	1707.50±111.50	0.55±0.26	7.41±1.98	85.35±1.68
RSNP6	3	1	0.1	20	0.2	1374.50±72.50	0.56±0.33	9.65±3.06	91.67±2.18

Abbreviations: RSNP, Rosuvastatin entrapped silica nanoparticles; TEOS, Tetraethyl orthosilicate; RSV, Rosuvastatin; PS, Particle size; PDI, Polydispersity index; ZP, Zeta potential; %DC, % drug content.

* Chitosan hydrochloride was dissolved in water (aqueous phase) while RSV was dissolved in propylene glycol (alcoholic phase). Following, the alcoholic solution was added to aqueous solution on stirring. TEOS was added dropwise to the hydroalcoholic solution.

* All concentrations were relevant to the final volume.

** Aqueous and alcoholic phases were mixed as volume ratios.

using UV spectrophotometry. Equal volumes of freshly prepared PBS were used to replace the withdrawn samples. Data obtained was analyzed to identify the pharmacokinetic release model (Zero order, Highuchi & Korsemeyer-Peppas) of the tested formulations. Moreover, % drug released after 24 h (Q_{24h}) and after 4 weeks (Q_{4w}) were calculated.

2.3.4. Transmission Electron Microscopy (TEM)

TEM was used to study the morphology of the selected formulation (RSNP2). A drop of the freshly prepared sample was appropriately diluted with distilled water, fixed onto a copper grid coated with carbon then left to dry in fresh air for 10 min. Following the sample was examined using TEM (Hitachi HF-2000, Tokyo, Japan) at 200 kV.

2.4. Preparation of Alginate-based Rosuvastatin Silica Nanoparticles Hydrogel Scaffolds (AL-RSNP)

Following the preparation of RSNP formulations, the optimum formulation was selected for the preparation of AL hydrogel. Briefly, accurately weighed amounts of AL (for a final concentration of 2% *w/v*) were slowly sprinkled onto the RSNP dispersion under magnetic stirring at 400 rpm and 37±0.2°*C*. for 15 min. Known volume of $CaCl_2$ aqueous solution was added to the dispersion (for a final concentration of 0.18% *v*/v) as one shot and was slowly hand-stirred for an additional 2 min. The resulting mixture was then removed from stirrer and immediately poured into circular molds (20 mm in diameter, 5 mm in height) and left to cross-link and solidify in fresh air for 20 min (Abasalizadeh et al., 2020; Eldeeb et al., 2022a). The resulting hydrogel scaffolds were carefully washed with distilled water to remove excess $CaCl_2$ and excess RSNP. Non-medicated AL-SNP was prepared using the same technique but without RSV.

2.5. Characterization of the prepared Alginate-based Rosuvastatin Silica Nanoparticles Hydrogel Scaffolds

2.5.1. In-vitro release testing

The in-vitro release characteristics of the AL-RSNP was determined using the dialysis bag method as previously mentioned under Section (2.3.3.) with minor modifications. The sample within the dialysis bag was replaced by accurate weighed fragment of AL-RSNP hydrogel (equivalent to 1 mg RSV). A volume of 1 mL PBS (pH 7.4) was added inside the bag, and it was tightly closed and immersed in a 90 mL glass bottle containing 50 mL PBS (pH 7.4) as the release medium. The test was continued as before and data obtained was analyzed to identify the pharmacokinetic release model (Zero order, Highuchi & Korsemeyer-Peppas) of the prepared scaffold. Finally, Q_{24h} and Q_{4w} were compared to those of the selected formulation.

2.5.2. In-vitro stability studies

Stability of the prepared AL-RSNP hydrogel was assessed in PBS as follows. First, swelling capacity (%W_s) was determined. Oven-dried hydrogel scaffolds were accurately weighed (W_0) and immersed in the buffer system at an incubator (temperature was set to 37±0.2°*C*). At the selected time intervals, the hydrogel samples were removed, blotted against filter papers, and reweighed (W_t). Swelling capacity (%W_s) was calculated using the following (Eldeeb et al., 2022a).

$$\%W_s = \frac{W_t - W_0}{W_0} \times 100$$

Secondly, % weight loss was assessed as follows. The fabricated AL-RSNP hydrogel scaffolds were accurately weighed, immersed in PBS, and reweighed daily until equilibrium weight was reached (W_m). Following, the examined samples were re-immersed in the buffer system and weighed repeatedly at preset time intervals (W_t) till complete degradation. % Weight loss was calculated using the succeeding equation (Akalin and Pulat, 2020; Bao et al., 2011).

$$\%\text{Weight loss} = \frac{W_m - W_t}{W_m} \times 100$$

2.5.3. Fourier transform infrared spectroscopy (FT-IR)

FT-IR was carried to identify any interactions between the ingredients in the selected formulation. Precisely sliced pieces of the selected hydrogel scaffold (AL-RSNP, 2 mg) were coated with potassium bromide and pressed into a disc. The same procedure was repeated for other ingredients. FT-IR spectra of the selected formulation (RSNP2), its physical mixture, the prepared hydrogel as well as all of the individual ingredients were all recorded using FT-IR spectrophotometer (Model, 8400 s Shimadzu, Kyoto, Japan) over the range of 4000–400 cm^{-1}.

2.5.4. Differential scanning calorimetry (DSC)

DSC was carried out to evaluate the thermal behavior of the scanned samples. Consequently, DSC analysis (DSC131 evo, Setaram Instrumentation, France) was run for the selected formulation (RSNP2), the prepared hydrogel (AL-RSNP) besides all of the individual components. Carefully sliced fragments of the scaffolds (2 mg) were placed in a hermetically sealed aluminum pan, heated through a range of 25–650°*C* (different for different materials analyzed) at a rate of 10°C/*min*. The procedure was the same for other individual ingredients.

2.5.5. Scanning Electron Microscopy (SEM)

SEM was used to study the surface morphology of the prepared AL-

RSNP hydrogel scaffold. Sample preparation involved fixing carefully sliced pieces from the selected hydrogel scaffold (2 mg) on stubs using carbon tape. Following, samples were sputter coated with a thin layer of gold (Quorum techniques Ltd., sputter coater, Q150t, England) and scanned with a Tescan SEM (Tescan Vega 3 SBU, Czech Republic) at voltage of 20 kV.

2.6. Gamma sterilization

Prior to in-vivo testing, the selected AL-RSNP hydrogel scaffold was sterilized using gamma irradiator (Gamma cell 1000; BEST Theratronics, Ontario, Canada) at a dose of 20 kGy. The irradiated hydrogel scaffolds were compared to their non-radiated analogues in terms of % DC and of release behavior via calculating the similarity factor (f_2) as follows (Costa, 2001).

$$f_2 = 50.log\left[\left\{1+\left(\frac{1}{n}\right)\sum_{t=1}^{n}(R_t - T_t)^2\right\}^{-0.5}.100\right].$$

Where, n represents the sample number, R_t represents % drug released before sterilization while T_t represents % drug released after the process.

2.7. Statistical analysis

All data was represented as mean values ± standard deviation. Data was analyzed using SPSS® software (SPSS Inc., 23.00 IBM Corporation, NY, USA) using one way analysis of variance (ANOVA) test coupled to least significant difference (LSD) to detect differences between samples ($n = 3$). Significance was detected at $P < 0.05$.

2.8. In-vivo testing

2.8.1. Animals and grouping

This study was performed in line with the principles of the Declaration of Helsinki. The study protocol was approved by the Research Ethics Committee at the Faculty of Pharmacy, Cairo University, Egypt (PI-3108). The followed procedures were in accordance with the Guide for the Care and Use of Laboratory Animals of the National Institutes of Health (NIH publication No.85–23, 1996). Twenty-seven healthy male adult New Zealand white rabbits, about 6 months old and 3.5–4 kg body weight, were conducted in the present study. The study was double-blinded (The veterinarian was not aware of the discs content and the analyst was not aware of the tissues to be examined). The animals were divided randomly into three main groups; GI, II and III (9 rabbits per each), each main group were subdivided into 3 subgroups (3 rabbits per each) according to observation periods; 1st, 2nd, and 3rd week.

2.8.2. Analgesia and surgical procedures

Directly prior to surgical procedures, each animal received an intramuscular meloxicam injection (1 mg/kg body weight) for preoperative analgesia together with a subcutaneous amikacin injection (5 mg/kg body weight) for perioperative antibiotic coverage. Ketamine hydrochloride (40 mg/kg body weight) and xylazine hydrochloride (7.5 mg/kg body weight) were used as intramuscular injections to induce anesthesia. The general anesthesia was maintained via 2% isoflurane/O_2 gas mixture administered via anesthetic mask (Carmel, 2012). The animals were laterally recumbent on the left side. The right perimandibular and cervical areas were prepared aseptically via shaving and scrubbing with Betadine then draping. Two milliliters of lidocaine (2%) were subcutaneously injected along the incision line (Young et al., 2008).

The inferior surface of the mandible was surgically incised from the chin perpendicularly to the gonial angles of the mandible. Also, a blunt dissection through the subcutaneous tissues down to the inferior border of the right hemimandible was carefully made. The periosteum was incised along the inferior border of the right hemimandible developing a subperiosteal flap. Following, the muscles and soft tissues' elevation and retraction were performed. Once, the lateral side of the mandible was visible, a partial thickness bony defect crossing through the lateral bony cortex, tooth roots, and trabecular bone in the premolar/molar area was created using a 10-mm trephine drill bit (Fig. 1). A root tip elevator was then used to remove the cortical and trabecular bone spicules besides the tooth roots. The tooth roots and trabecular bone were extracted as an articulate mass, consistently revealing the cortical bone of the medial plate. Any remaining bony debris were removed from the defect with a curette under profuse irrigation with saline solution. The defect was left without treatment in GI (Control), while it was stuffed with plain hydrogel disc (without RSV) in GII, and with the fabricated AL-RSNP hydrogel in GIII. Then, the muscle and subcutaneous layers were closed with continuous resorbable 4–0 Vicryl sutures and the skin closed with interrupted 4–0 Vicryl sutures.

2.8.3. Postoperative care

Two subcutaneous injections of meloxicam (1 mg/kg) were given daily after surgery for continued postoperative analgesia and Amikacin (5 mg/kg) was continued for 4 days postoperatively. The wound was dressed daily and checked for inflammation, seroma and infection. Food and water were given ad libitum, where the animals received a soft diet for 3 days after surgery, then the regular diet of hard pellets was introduced.

2.8.4. Euthanasia and postoperative evaluation

Animals of each subgroup were scarified after general anesthesia at the end of each successive observation period (1st, 2nd, and 3rd week post-operation). The operated mandibles were harvested with soft tissue excision, exposing the bony defect. The defect was evaluated visually then the collected bones were fixed in 10% neutral buffered formalin solution for 1 week. Following, the samples were decalcified by 10% formic acid, trimmed, washed with water, dehydrated with ethyl alcohol, cleaned with xylene, and embedded in pre-heated paraffin (preheated in hot air oven at 56°C for 24 h). Thin sections of about 4–6 μm were processed and stained with Hematoxylin and Eosin stain and examined under light microscope (CX21 Olympus microscope, Tokyo, Japan).

3. Results and discussion

3.1. Characterization of the prepared silica nanoparticles (SNPs)

Two variables were tested during the preparation of RSNP, namely, aqueous: alcoholic phase ratio and the concentration of TEOS. Below are the different characterization tests to identify the significance (if any) of one or both variables.

3.1.1. Particle Size (PS), Zeta Potential (ZP), and Polydispersity Index (PDI) measurements

Analysis of PS of the prepared formulations revealed that increasing aqueous: alcoholic ratio led to significant increase in PS ($P < 0.05$). Increasing water and decreasing alcohol proportions resulted in a reduced availability of alcohol to react with TEOS and an increase in the immiscibility gap between the hydroalcoholic solution and TEOS. This, in turn, left large amounts of TEOS unreacted in the solution and caused larger particles to be detected (Lu and Owens, 2018; Donatti et al., 2002). On the other hand, increasing TEOS concentration caused significant reduction in PS ($P < 0.05$) which might be attributed to increased TEOS available to interact with alcohol and undergo polycondensation with chitosan hydrochloride to form siloxane bond (Zaghloul et al., 2022). Upon thorough inspection, it was found that in the water: alcohol ratio of 3: 1 (v/v), the PS was much larger (micron range) when compared to the 1: 1 or even the 2: 1 (v/v). That means that in the 3: 1 (v/v), the alcohol amount was too small to assist hydrolysis

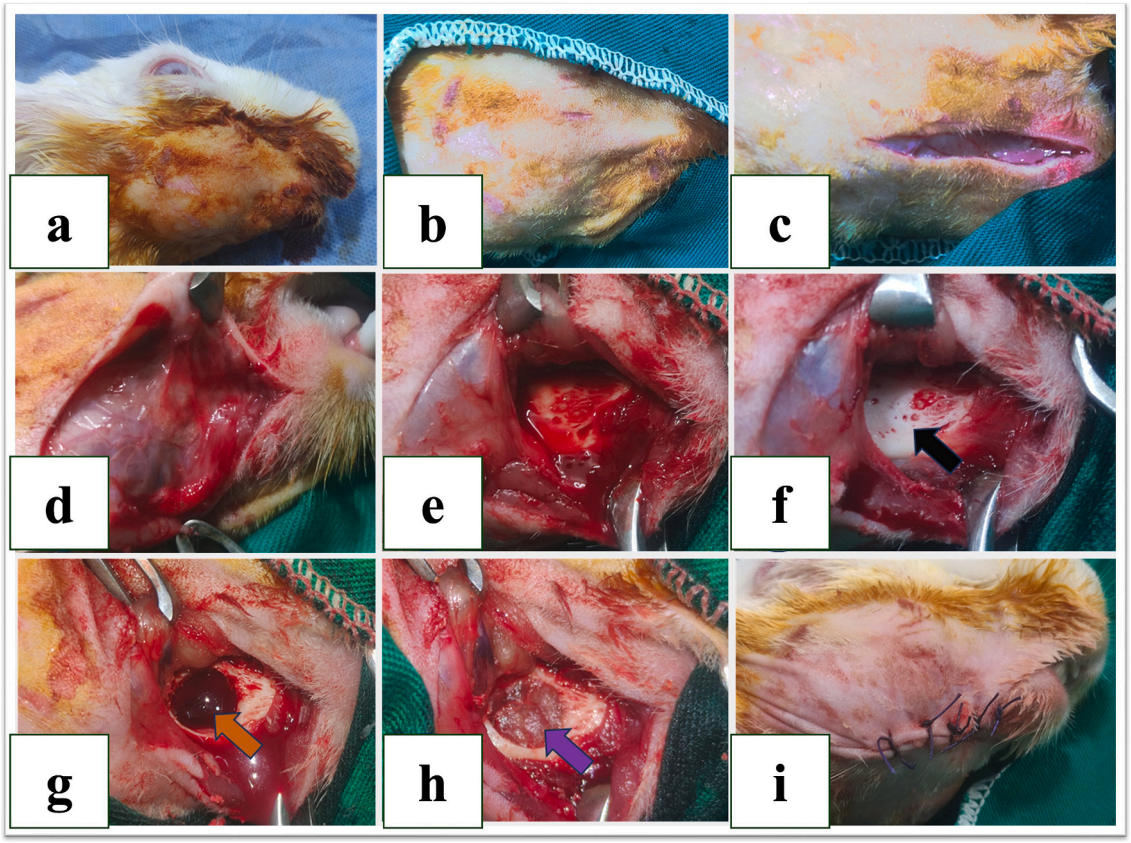

Fig. 1. Photographs showing the surgical procedures as: (a, b) aseptic preparation of mandibular area (c, d) surgical incision and blunt dissection till reach periosteum, (e, f) periosteum was incised developing a subperiosteal flap and muscles and soft tissues elevation and retraction. The lateral side of the mandible was visible (black arrow), (g) a 10-mm a partial thickness bony defect crossing through the lateral bony cortex, tooth roots, and trabecular bone in the premolar/molar area (orange arrow). (h) filling the mandibular defect with alginate-based hydrogel scaffold loaded with rosuvastatin silica nanoparticles (AL-RSNP) (purple arrow), (i) surgical wound and skin closure with Vicryl 4/0. (For interpretation of the references to color in this figure legend, the reader is referred to the web version of this article.)

and polycondensation to form sufficient RSNP.

PDI values ranged between 0.387±0.02 to 0.63±0.15 which indicates that particle size distribution was sufficiently uniform through all the formulations (Danaei et al., 2018). ZP values ranged between 7.41±1.98 to 12.90±2.80. Such positive charge could be attributed to the presence of Ch (Mohammed et al., 2017). The results of PS, PDI and ZP values can be seen in Table 1.

3.1.2. Drug content (% DC)

From the data in Table 1, % DC for all the prepared formulations was found to range from 85.35±1.68 to 100.22±0.67% indicating there was minimal drug loss during the formulation process. As water: alcohol ratio decreased, % DC increased (RSNP1 > RSNP3 > RSNP5; $P < 0.05$). Additionally, as TEOS concentration increased, an increase in % DC was observed (RSNP2 > RSNP1, RSNP4 > RSNP3 and RSNP6 > RSNP5; $P < 0.05$). The findings correlate with those of PS, whereas a decrease in hydrophilicity and increase in TEOS allowed for increased rate of RSNP formation and consequently more RSV being entrapped.

3.1.3. In-vitro release testing

As revealed from the data in Table 2 and can be seen from Fig. 2, the release of RSV from all RSNP formulations followed a biphasic pattern. A

Table 2
In-vitro release testing of RSNP Formulations.*

Formulation Code*	Amount Released (%)		Release Model				
	Q_{24h}	Q_{4w}	Zero	Diffusion	Korsmeyer-Peppas		
			r^2	r^2	r^2	k	n
RSNP1	30.13±0.40	95.31±1.67	0.859±0.007	0.971±0.001	0.984±0.006	7.298±0.027	0.404±0.002
RSNP2	27.29±2.36	98.72±0.52	0.891±0.002	0.984±0.002	0.987±0.005	6.730±0.108	0.417±0.004
RSNP3	32.00±2.44	90.52±1.22	0.869±0.011	0.974±0.007	0.989±0.003	10.000±2.353	0.343±0.043
RSNP4	32.67±1.75	96.61±0.36	0.877±0.008	0.971±0.005	0.972±0.018	9.369±0.458	0.358±0.010
RSNP5	28.59±0.58	86.28±9.47	0.866±0.007	0.976±0.004	0.976±0.003	10.170±1.224	0.334±0.005
RSNP6	31.18±0.16	89.92±1.58	0.826±0.018	0.956±0.007	0.978±0.001	9.827±0.070	0.351±0.005
AL-RSNP	22.56±2.11	81.52±4.81	0.842±0.013	0.968±0.005	0.986±0.004	6.399±0.106	0.408±0.006

Abbreviations: RSNP, Rosuvastatin-entrapped silica nanoparticles; AL-RSNP, Alginate-loaded rosuvastatin-entrapped silica nanoparticles; Q_{24h}, % drug released after 24 h; Q_{4w}, % drug released after 4 weeks.

* The composition of the prepared RSNP is found in Table 1. AL-RSNP is composed of Alginate matrix loaded with the selected Rosuvastatin-entrapped silica nanoparticle (RSNP2).

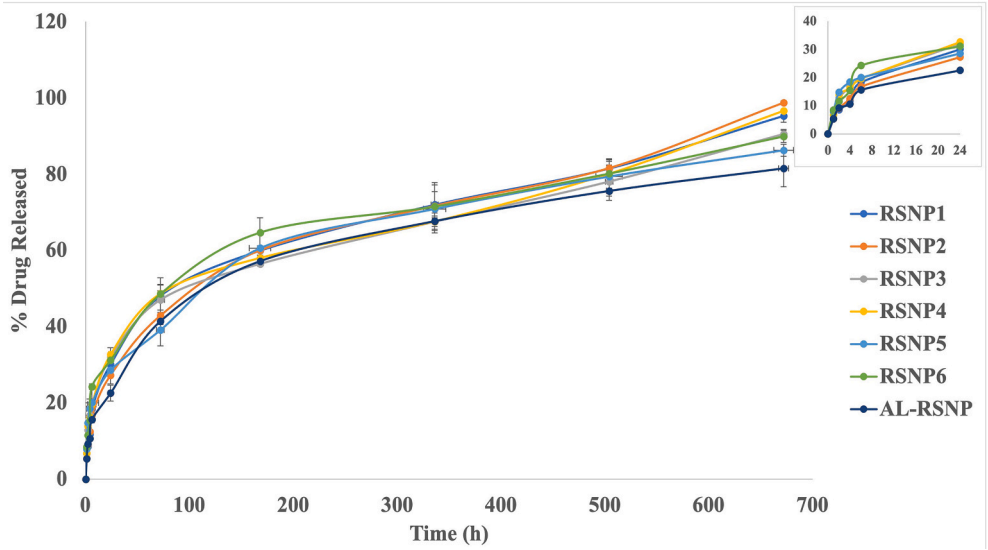

Fig. 2. Release profiles of the prepared rosuvastatin silica nanoparticles as well as the fabricated alginate-based hydrogel scaffold loaded with rosuvastatin silica nanoparticles in phosphate buffer saline (pH 7.4) at 37±0.2°*C*.

burst effect can be clearly seen in the initial 24 h (Q_{24h}), responsible for the release of 27.29±2.36 to 32.67±1.75% of RSV load from the surface layers. The initial burst release was followed by a sustained release pattern (up to 4 weeks) attributed to the slow diffusion of RSV from the cores of the formed SNPs. The amount of RSV released at the 4-week mark (Q_{4w}) ranged between 81.52±4.81 to 98.72±0.52%. Biphasic release pattern is characteristic of most nanoparticle delivery systems and SNPs are no exception (Mohseni et al., 2015). Meanwhile, around 97.26±0.40% RSV was released from its suspension after 1 h, suggesting the suitability of the dialysis membrane used.

From the data in Table 2, it was found that all formulations follow Korsmeyer-Peppas model with r^2 values ranging between 0.972±0.018 and 0.989±0.003 while n values, ranging from 0.334±0.005 to 0.417±0.004, indicating fickian diffusion was the predominant release mechanism. One interesting note is that the release constant value (k) was directly proportional to PS values. Such correlation was apparent both on decreasing aqueous: alcoholic ratio (RSNP1 < RSNP3; $P < 0.05$ and RSNP3 < RSNP5; $P > 0.05$) and on increasing TEOS concentration (RSNP2 vs RSNP1; $P > 0.05$, RSNP4 vs RSNP3; $P < 0.05$ and RSNP6 vs RSNP5; $P < 0.05$). From one hand, decreased hydrophilicity and increased alcohol content infer a reduction in the immiscibility gap between the hydroalcoholic solution and TEOS. On the other hand, increasing TEOS concentration allows for higher rates of hydrolysis, nucleation, and polycondensation. Both events led to increased formation of SNPs with smaller PS and larger RSV content within the core layers. Since the release of RSV was determined to depend on the diffusion from the core, decreasing PS was coupled with slower overall release.

Based on the results of PS measurements and in-vitro release, RSNP2 was selected for further evaluation. It possessed the smallest PS (221.00±7.30 nm) while maintaining the most efficient drug release kinetics as indicated by the smallest k (6.730±0.108).

3.1.4. *Transmission Electron Microscopy (TEM)*

TEM image of RSNP2 is displayed in Fig. 3. As can be seen from the figure, SNP with non-uniform spherical shape could be observed. The detected particle was well-dispersed.

3.2. *Characterization of the prepared Alginate-based Silica Nanoparticles (AL-RSNPs)*

The selected formulation (RSNP2) was entrapped in AL matrix and prepared as hydrogel scaffold which was further evaluated.

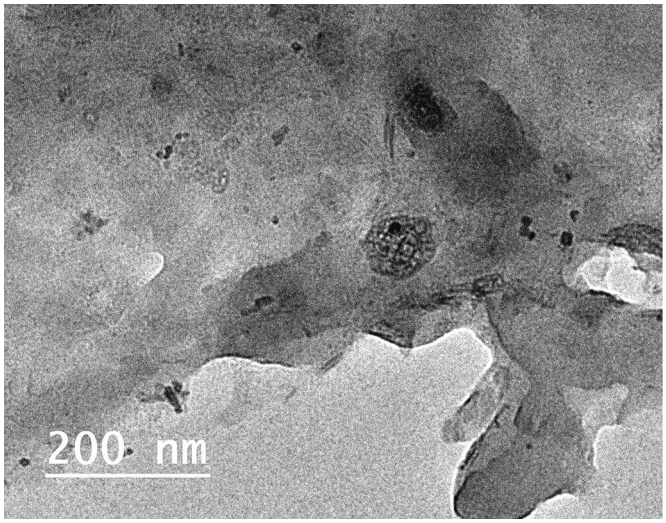

Fig. 3. TEM image showing the morphology of the selected rosuvastatin loaded silica nanoparticles (RSNP2).

3.2.1. *In-vitro release testing*

In-vitro release was repeated on the new AL-RSNP hydrogel scaffolds to check for alterations (if any) in the release behavior from the original RSNP2. As evident by the data in Table 2 and the curve in Fig. 2, RSV in the double entrapment system followed a bi-phasic release pattern similar to that of free RSNP formulations. The main difference however is that the double entrapment led to a significant reduction ($P < 0.05$) in the initial burst release (Q_{24h} was 22.56±2.11% for AL-RSNP vs 27.29±2.36% for RSNP2). Similarly, Q_{4w} was significantly lowered ($P < 0.05$) in AL-RSNP (81.52±4.81%) against that of RSNP2 (98.72±0.52%). The newly formed system is a dual-nanoparticle-hydrogel system, imposing a double-barrier system for RSV to cross. Addition of extra barrier (AL matrix) elongates the path crossed by RSV from the core of RSNP to the release medium which hinders drug release and is solely responsible for the reduction in Q_{24h} and Q_{4w} values.

Korsemeyer-Peppas was established as the kinetic model that best describes the release of RSV from AL-RSNP scaffold, where r^2 =

0.986±0.004 and n = 0.408±0.006, suggestive of fickian diffusion as the predominant release mechanism. Such results were similar to those of RSNP2, indicating that the loading of the RSNP2 within AL matrix didn't affect the release mechanism. The Korsemeyer-Peppas constant (k) decreased (6.399±0.106 for AL-RSNP vs 6.730±0.108 for RSNP2; $P < 0.05$) which is in agreement with the delay of release upon entrapping within AL matrix.

3.2.2. In-vitro stability studies

The in-vitro stability studies are essential in evaluating the effect of water on the fabricated hydrogel. Upon contact with water, hydrogels tend to absorb water, polymer chains are relaxed, and the hydrogel matrix swells (Chai et al., 2017; Eldeeb et al., 2022b). After certain swelling threshold, the hydrogel starts to degrade until the whole system collapses. Generally, the ability of the hydrogel to swell facilitates exchange of O_2, nutrients and other agents loaded within the matrix while auto-degradation enhances its safety profile and reduces the hassle of surgical removal after some period of time (Nan et al., 2019; Adel et al., 2021). On analysis of the fabricated hydrogel (AL-RSNP), it possessed a swelling capacity of 78.02±2.64% after 2 weeks of immersion in PBS before reaching equilibrium. Such moderate swelling capacity can be attributed to the entrapment of RSNPs within the pores, leaving less space for water molecules to diffuse through. On the other hand, following equilibrium, the hydrogel started to degrade, reaching % weight loss of 28.77±0.99% at the 3-week mark, before it completely degraded thereafter.

3.2.3. Fourier transform infrared spectroscopy (FT-IR)

FT-IR spectra of all ingredients as well as of AL-RSNP hydrogel can be seen in Fig. 4. In the spectrum of RSV, a characteristic broad band at 3372 cm^{-1} is attributed to carboxylic OH group while the peak at 1551 cm^{-1} was due to the stretching CO group. Other absorption peaks can be seen at 1381 and 1153 cm^{-1} due to the asymmetric and symmetric stretching sulfoxide group (T. A and A. MS, 2016; Sarfraz et al., 2017). The spectrum of Ch reveals broad band at 3287 cm^{-1} due to the stretching of both OH and NH_2 groups. At the same time, the broad band at 2881 cm^{-1} is due to the stretching CH_2 aliphatic group while the peaks at 1655 and 1157 cm^{-1} representative of the vibrational amide group and the stretching C-O-C group (Varma and Vasudevan, 2020). TEOS spectrum revealed absorption peaks at 2978 and 1107 cm^{-1} representative of stretching CH aliphatic and CO groups, respectively (Rubio et al., 1998). As for AL, its spectrum reveals a characteristic broad band at 3352 cm^{-1} due to OH group while the stretching vibrational peak at 2932 cm^{-1} is caused by CH aliphatic. Other peaks include the asymmetric and symmetric stretching vibration at 1593 cm^{-1} and 1416 cm^{-1} due to carboxylate group as well as the stretching vibration of CO at 1033 cm^{-1} (Bajas et al., 2021). Investigating the spectrum of RSNP2 revealed the following. The stretching CH_2 peak of Ch at 2881 cm^{-1} is present but those of the amide and C-O-C groups were shifted to a lower wavelength at 1647 and 1080 cm^{-1}, respectively. Similarly, stretching peak of CO group of TEOS was shifted to 1045 cm^{-1}. Such revelation might be attributed to the interaction between Ch and TEOS and the formation of silanol group in the newly formed SNPs. That can be confirmed by the appearance of several new peaks at 837, 991 and 1138 cm^{-1} representative of the symmetric stretching Si-O-Si (siloxane), the stretching Si-OH (silanol) and the asymmetric stretching Si-O-Si groups, respectively (Panwar et al., 2015). On the other hand, the spectrum of the physical mixture of RSNP2 revealed the same peaks of individual ingredients albeit at reduced intensity due to dilutional effects. In the spectrum of AL-RSNP hydrogel, the characteristic peaks of the symmetric stretching Si-O-Si, stretching silanol and asymmetric stretching Si-O-Si groups, respectively, are present but with reduced intensity due to dilution of RSNP2 in AL matrix. On the other hand, the broad band of OH group of AL was shifted to 3383 cm^{-1}, suggesting possible hydrogen bond interaction between the AL matrix and the loaded RSNPs as well as ionic interaction with calcium ions (Adel and ElKasabgy, 2014).

3.2.4. Differential scanning calorimetry (DSC)

Thermograms of the investigated samples are shown in Fig. 5. For RSV, a sharp endothermic peak at 84°C is characteristic of the drug and is caused by water loss (Shiralashetti et al., 2014; González et al., 2022). In Ch thermogram, two characteristic peaks are visible, an endothermic peak at 96°C and an exothermic one at 222°C representative of water loss and decomposition, respectively (Zhao et al., 2021). In the thermogram of AL, a broad endothermic peak is seen at 125°C corresponding to loss of water while the two broad exothermic peaks at 246 and 275°C represent a two-step decomposition (Rao et al., 2013; Abulateefeh and Taha, 2014; Rhimi et al., 2022). The thermogram of RSNP2 reveals a broad endothermic peak at 114°C due to loss of physisorbed water. In the thermogram of the selected scaffold (AL-RSNP), all of the characteristic peaks of RSV and Ch disappeared while a new peak appeared at 132°C representing moisture desorption from the formulated hydrogel while the sharp endothermic peak at 201°C is brought by the melting of AL. (Padma et al., 2018)

3.2.5. Scanning Electron Microscopy (SEM)

Fig. 6. represents the SEM images of AL-RSNP hydrogel scaffold. The images show clearly the typical intertwining network of hydrogel scaffolds owing to polymer chains entanglement. On polymer rigidification and crosslinking, a porous but extremely dense surface of networks has formed. This porous structure is essential for assisting the healing process (Elkasabgy et al., 2018).

3.3. Gamma sterilization

The % DC of sterilized AL-RSNP hydrogel remained above 90% (95.97±1.01%) and was insignificantly different ($P > 0.05$) from the non-radiated hydrogel (% DC = 97.60±1.40%). As for the similarity factor (f_2), it was calculated upon completion of the release profile of the irradiated hydrogel and was equal 86.05±5.69, indicating there were no difference in release pattern owing to the irradiation process. Generally, when f_2 is >50, the 2 hydrogels are considered in-vitro similar (Costa, 2001). Therefore, the sterilization method used preserved the physicochemical characteristics of the scaffold. Similar results were mentioned elsewhere (Abo Elela et al., 2017).

3.4. In-vivo testing

3.4.1. Visual evaluation

The results of macroscopic evaluation can be seen in Fig. 7. and it summarizes as follows. At the end of the 1st week, a clear hematoma could be seen in the control group (GI) that was slightly raised above bone level. At the same time, in all other groups, the defect sites were filled with hemorrhagic areas and remnants of hydrogel discs. At the 2-week mark, the defect areas were noticed in GI and GII with ease but were hardly identified in GIII. Fibrous connective tissues started to form and were clearly visible in all groups albeit its level was slightly different among different groups. It was seen below the defect level in GI, at the defect level in GII and glistering above the defect level in GIII. By the end of the 3rd week, in GI, the defect site almost disappeared and was filled with whitish fibrous tissue that was raised above the bone surface. In the other groups, defect sites were hardly identified and stuffed with hard fibrous tissue. In GIII, the fibrous tissue was cartilaginous and homogenous in color.

Overall, the drug-laden hydrogel (AL-RSNP; GIII) was superior in restoring the normal structure of the bony fibrous tissue at a faster rate than other groups while the resulting tissue was harder and more homogenous in color.

3.4.2. Microscopical examination

Images of microscopical examination can be seen in Fig. 8. At the end

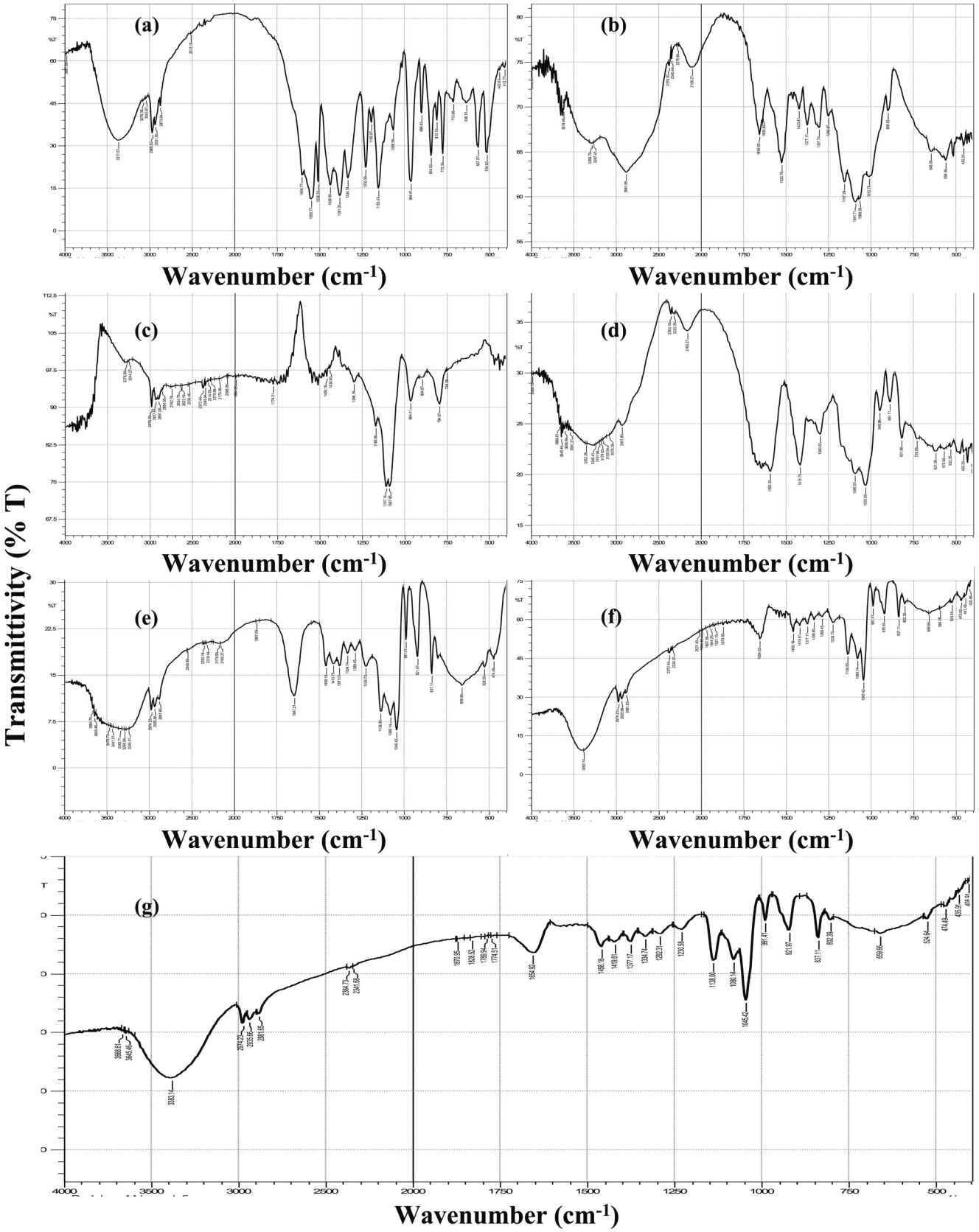

Fig. 4. FT-IR spectra of (a) Rosuvastatin, (b) Chitosan HCl, (c) Tetraethyl orthosilicate, (d) Sodium Alginate, (e) The selected rosuvastatin silica nanoparticle (RSNP2), (f) Physical mixture of RSNP2, (g) Alginate-based hydrogel scaffold loaded with rosuvastatin silica nanoparticles (AL-RSNP).

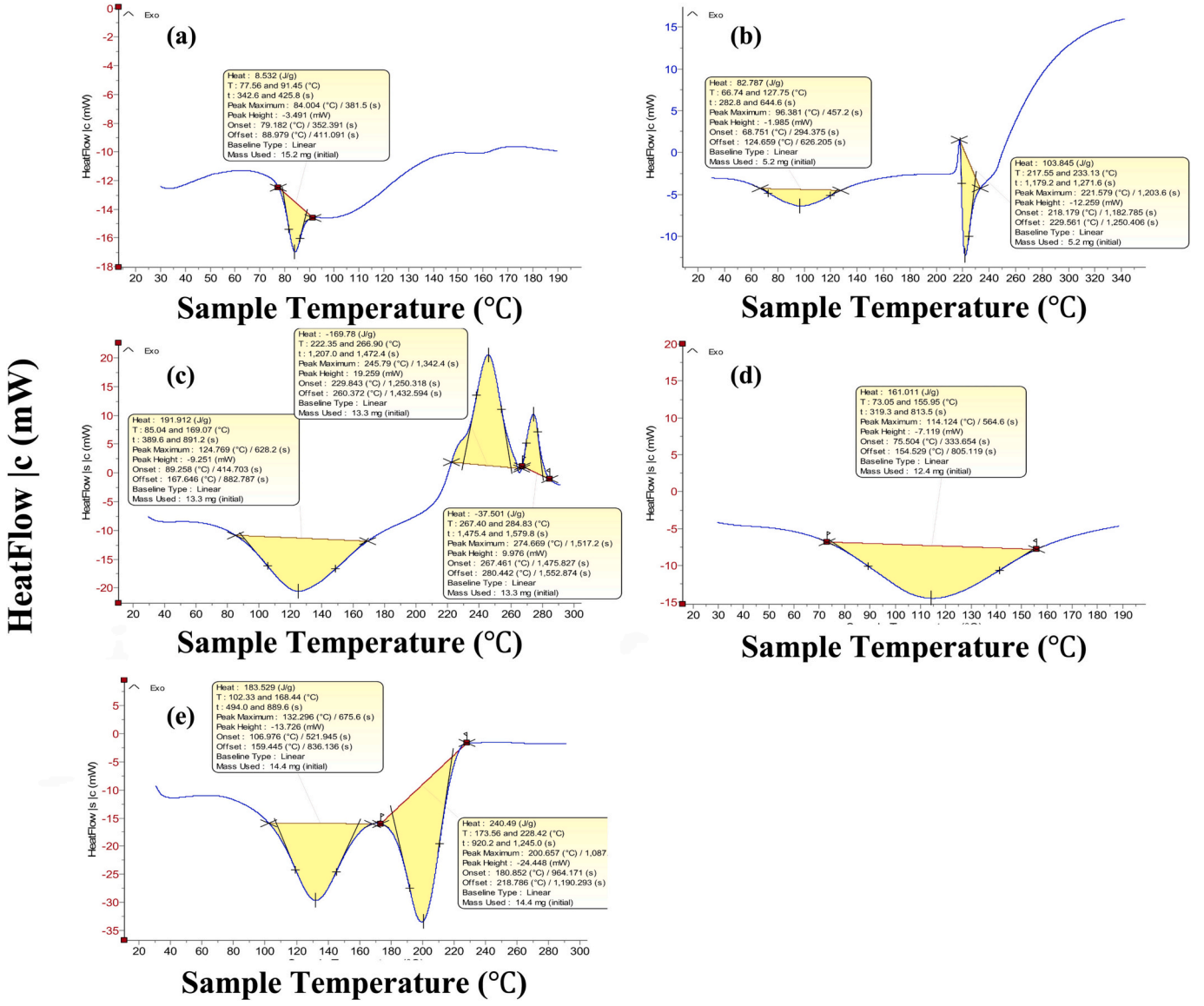

Fig. 5. DSC thermograms of (a) Rosuvastatin, (b) Chitosan HCl, (c) Sodium Alginate, (d) The selected rosuvastatin silica nanoparticle (RSNP2), (e) Alginate-based hydrogel scaffold loaded with rosuvastatin silica nanoparticles (AL-RSNP).

of the 1st week, formation of fibrous connective tissue started in all groups with signs of hemorrhage and infiltration by mononuclear inflammatory cells (stars). Necrotic tissue was evident at the control group (GI; black arrowhead). At the 2-week mark, larger numbers of inflammatory cells infiltrated the defect tissues in all groups (stars) and necrotic tissue was spotted in the blank hydrogel group (GII; black arrowhead). Osteoblasts formation began in treatment group (GIII; red arrowhead). By the end of the 3rd week, all groups showed evidence of fibrous tissue with infiltration by inflammatory cells (stars). It is worth mentioning that GIII lacked any signs of necrotic tissue during the 3-week testing period. Newly formed bony tissue was only observed in GIII (green arrowhead).

To conclude, the drug-loaded hydrogel (AL-RSNP; GIII) demonstrated enhanced rate of healing and bone tissue formation that was similar in structure to the original tissue, as was evident by osteoblasts appearance at the end of the 2nd week, bones visualization by the end of the 3rd week and absence of necrotic tissue.

4. Conclusion

Intrinsic ability of the body to heal damaged tissue is of utmost importance in mammalian survival. Nevertheless, the process is slow and very poor in restoring severely damaged tissues to their original structure and function. That have led to the emergence of tissue engineering (TE) where a scaffold is constructed and loaded with cells, bioactive cues, chemical agents, … etc., and implanted in the defect area to restore the normal structure and function of the tissue. Rosuvastatin (RSV) has long been used as cholesterol lowering agent. Similar to other statins, it has shown promising potential as a stimulant of tissue regeneration. Silica nanoparticles (SNPs) offer the advantages of traditional nanoparticles named, small particle size, large surface area, enhanced cellular uptake and adds to that the biocompatibility and lack of toxic residues. The goal of this research was to assess the efficacy of RSV in bone TE while at the same time, achieving a sustained drug delivery to the target tissue. That was made possible through incorporation of the drug within SNPs followed by loading the RSNPs into alginate hydrogel scaffold (AL-RSNP). The selected formulation (RSNP2) was composed of RSV dissolved in PG (0.2% *w/v*) and Ch dissolved in

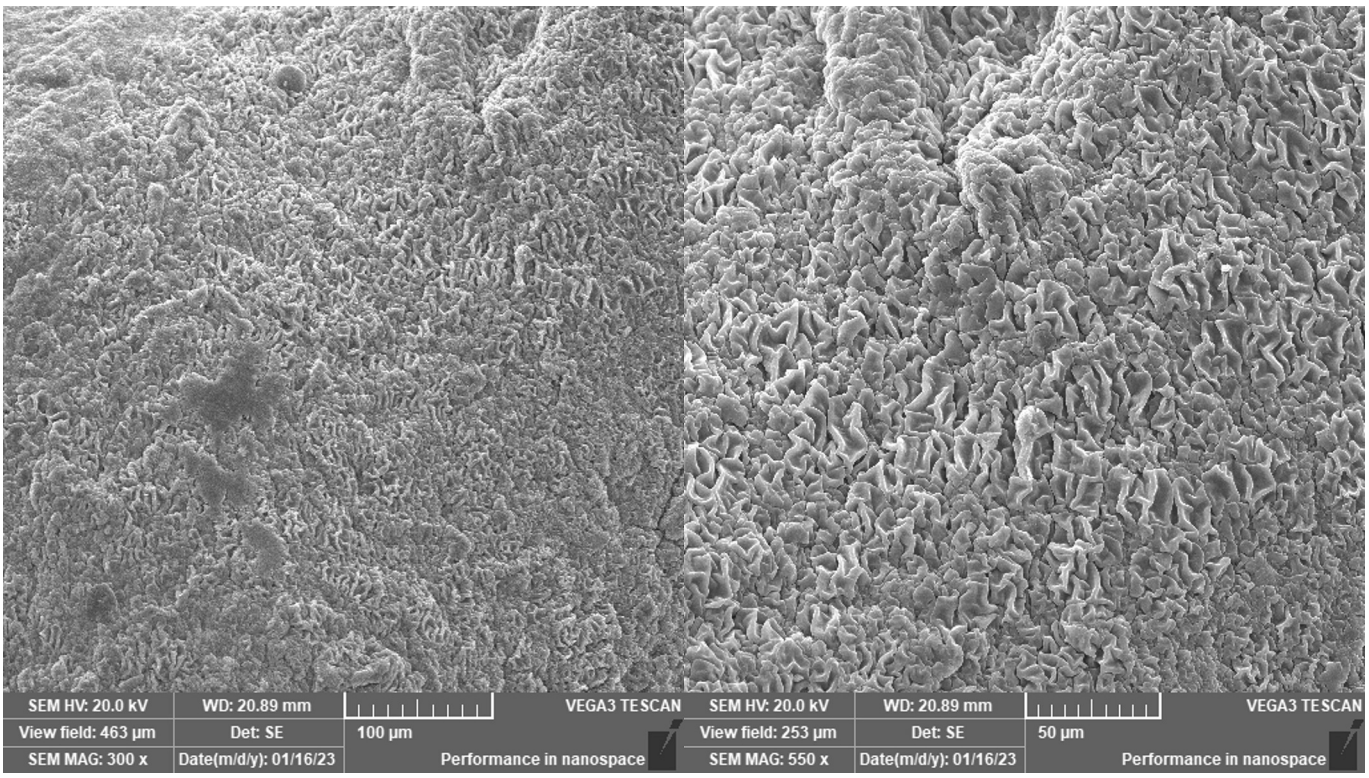

Fig. 6. Surface morphological examination using SEM of the alginate-based hydrogel loaded with rosuvastatin silica nanoparticles (AL-RSNP).

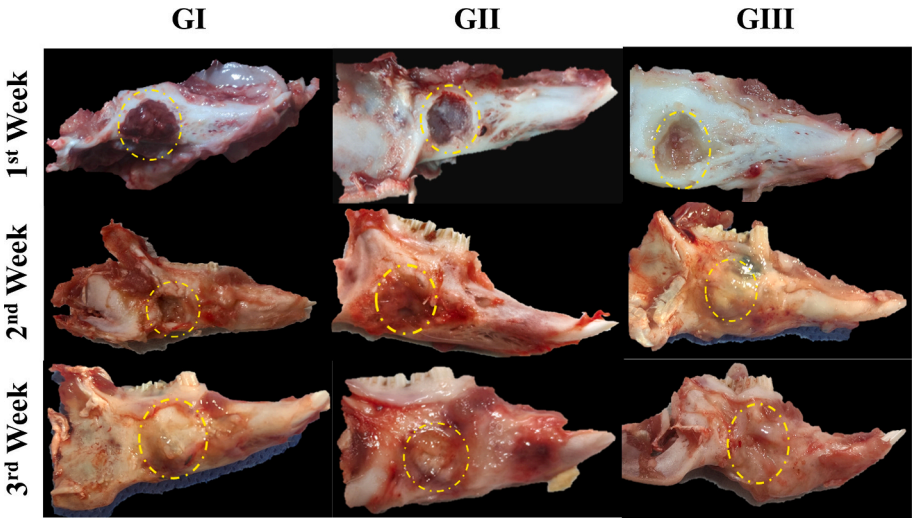

Fig. 7. Visual evaluation of the defect area of jawbones of New Zealand rabbits in 4 different groups over 3 weeks period. Groups include G1 (Control), GII (plain hydrogel with no drug), and GIII (alginate-based hydrogel loaded with rosuvastatin silica nanoparticles, AL-RSNP).

aqueous phase (0.1% w/v) in a ratio of 1 (alcoholic phase): 1 (aqueous phase). TEOS was added to the hydroalcoholic solution as silica source (20% *v*/v). RSNP2 possessed small particle size and exhibited sustained release pattern up to 4 weeks. Following, AL-RSNP hydrogel scaffold was characterized in-vitro using FT-IR and DSC that showcased the formation of nanoparticles, crosslinking of the polymer and thermal behavior of the hydrogel. SEM images illustrated the porous and extremely dense surface of the formulated AL-RSNP hydrogel scaffold. The results of in-vivo testing revealed the enhanced bone tissue formation achieved with AL-RSNP. The newly formed tissue was homogenous in color and similar to the original tissue in structure. Future translational research can be conducted to expand the use of the developed formulation in clinics.

Funding

The authors declare that no funds, grants, or other support were received during the preparation of this manuscript.

CRediT authorship contribution statement

Islam M. Adel: Conceptualization, Methodology, Software, Formal analysis, Investigation, Resources, Writing – original draft, Writing – review & editing. **Mohamed F. ElMeligy:** Conceptualization,

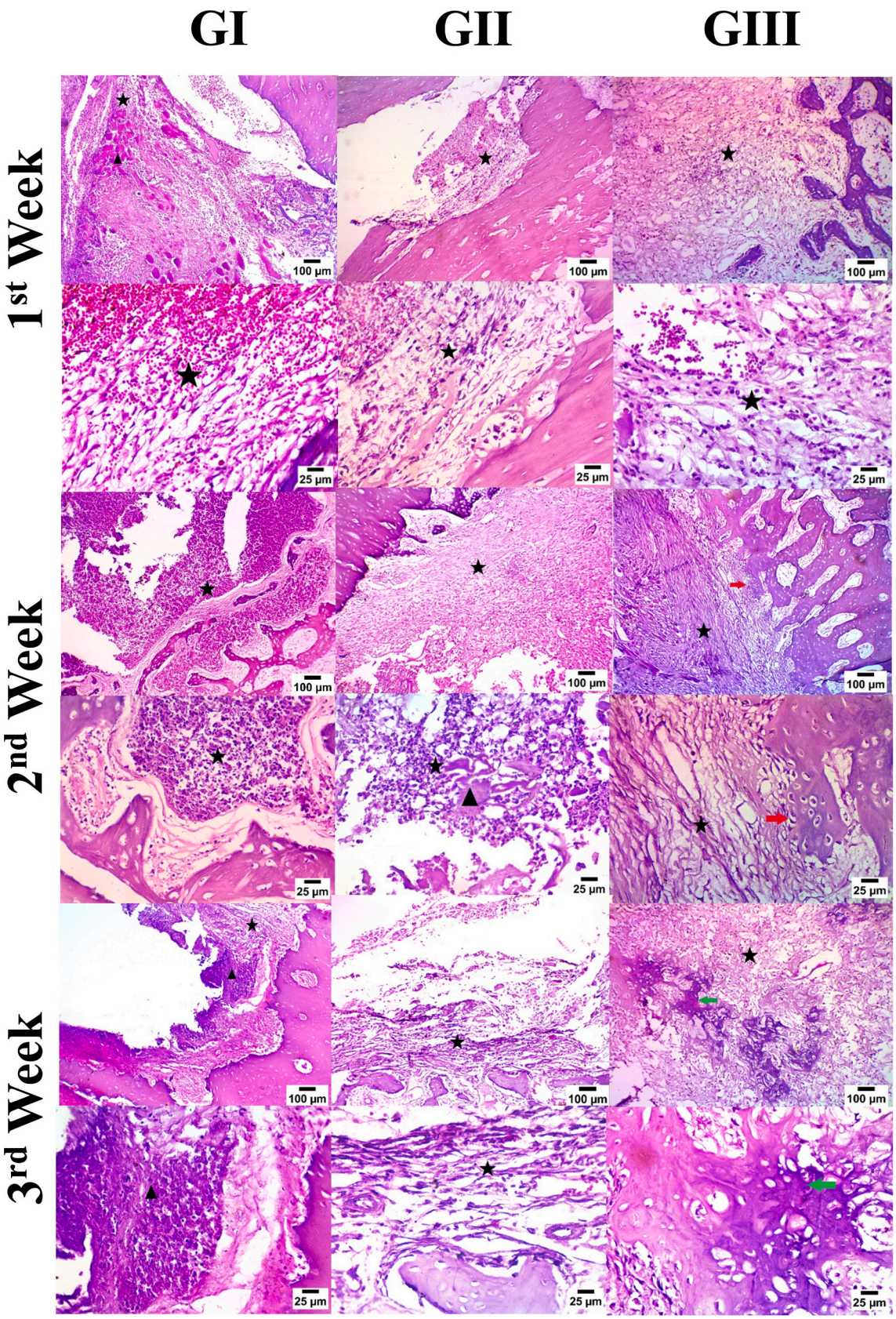

Fig. 8. Microscopical examination of the new jawbone tissue of New Zealand rabbits in 4 different groups over 3 weeks period. Groups include G1 (Control), GII (plain hydrogel with no drug), and GIII (alginate-based hydrogel loaded with rosuvastatin silica nanoparticles, AL-RSNP).

Methodology, Resources. **Mohammed S. Amer:** Methodology, Resources. **Nermeen A. Elkasabgy:** Conceptualization, Methodology, Software, Formal analysis, Investigation, Resources, Writing – original draft, Writing – review & editing, Supervision.

Declaration of Competing Interest

The authors declare the following financial interests/personal relationships which may be considered as potential competing interests.

Islam M. Adel reports equipment, drugs, or supplies was provided by Ellebedy Fellowship.

Data availability

The datasets generated during and/or analyzed during the current study are available from the corresponding author on reasonable request.

Acknowledgment

Islam M. Adel was supported by the Ellebedy Fellowship for Young Scientists. Also, we would like to acknowledge Islam Elgohary, a researcher assistant of molecular pathology in Animal Health Research Institute at Elgohary pathology laboratory, for his tremendous contributions in the histopathological assessment segment.

References

Abasalizadeh, F., et al., Mar. 2020. Alginate-based hydrogels as drug delivery vehicles in cancer treatment and their applications in wound dressing and 3D bioprinting. J. Biol. Eng. 14, 8. https://doi.org/10.1186/s13036-020-0227-7.

Abd-Elal, R.M.A., et al., 2023. Formulation, optimization, in-vivo biodistribution studies and histopathological safety assessment of duloxetine HCl-loaded ultra-elastic nanovesicles for antidepressant effect after intranasal and transdermal delivery. Int. J. Pharm. X 6, 100194. https://doi.org/10.1016/j.ijpx.2023.100194.

Abo Elela, M.M., ElKasabgy, N.A., Basalious, E.B., 2017. Bio-shielding in Situ Forming Gels (BSIFG) Loaded with Lipospheres for Depot Injection of Quetiapine Fumarate: in Vitro and in Vivo Evaluation. AAPS PharmSciTech 18 (8), 2999–3010. https://doi.org/10.1208/s12249-017-0789-y.

Abulateefeh, S., Taha, M., 2014. Enhanced drug encapsulation and extended release profiles of calcium–alginate nanoparticles by using tannic acid as a bridging cross-linking agent. J. Microencapsul. https://doi.org/10.3109/02652048.2014.985343. Nov.

Adel, S., ElKasabgy, N.A., 2014. Design of innovated lipid-based floating beads loaded with an antispasmodic drug: in-vitro and in-vivo evaluation. J. Liposome Res. 24 (2), 136–149. Jun. https://doi.org/10.3109/08982104.2013.857355.

Adel, I.M., ElMeligy, M.F., Abdelkhalek, A.A., Elkasabgy, N.A., 2021. Design and characterization of highly porous curcumin loaded freeze-dried wafers for wound healing. Eur. J. Pharm. Sci. 164, 105888. https://doi.org/10.1016/j.ejps.2021.105888.

Adel, I.M., ElMeligy, M.F., Elkasabgy, N.A., 2022. Conventional and Recent Trends of Scaffolds Fabrication: A Superior Mode for Tissue Engineering. Pharmaceutics 14 (2). https://doi.org/10.3390/pharmaceutics14020306.

Akalin, G.O., Pulat, M., 2020. Preparation and characterization of κ-carrageenan hydrogel for controlled release of copper and manganese micronutrients. Polym. Bull. 77 (3), 1359–1375. https://doi.org/10.1007/s00289-019-02800-4.

Arriagada, F.J., Osseo-Asare, K., 1995. Synthesis of Nanosize Silica in Aerosol OT reverse Microemulsions. J. Colloid Interface Sci. 170 (1), 8–17. https://doi.org/10.1006/jcis.1995.1064.

Bajas, D., et al., 2021. Formulation and Characterization of Alginate-Based Membranes for the Potential Transdermal Delivery of Methotrexate. Polymers (Basel) 13 (1). https://doi.org/10.3390/polym13010161.

Bao, Y., Ma, J., Li, N., 2011. Synthesis and swelling behaviors of sodium carboxymethyl cellulose-g-poly(AA-co-AM-co-AMPS)/MMT superabsorbent hydrogel. Carbohydr. Polym. 84 (1), 76–82. https://doi.org/10.1016/j.carbpol.2010.10.061.

Battafarano, G., et al., 2021. Strategies for Bone Regeneration: From Graft to Tissue Engineering. Int. J. Mol. Sci. 22 (3) https://doi.org/10.3390/ijms22031128.

Beck, G., et al., 2011. Bioactive silica based nanoparticles stimulate bone forming osteoblasts, suppress bone esorbing osteoclasts, and enhance bone mineral density in vivo. Nanomedicine 8, 793–803. Nov. https://doi.org/10.1016/j.nano.2011.11.003.

Bondareva, J., et al., 2020. Environmentally Friendly Method of Silicon Recycling: Synthesis of Silica Nanoparticles in an Aqueous Solution. ACS Sustain. Chem. Eng. https://doi.org/10.1021/acssuschemeng.0c03783. Vol. XXXX, Aug.

Brydone, A., Meek, D., Maclaine, S., 2010. Bone grafting, orthopaedic biomaterials, and the clinical need of bone engineering. Proc. Inst. Mech. Eng. H 224, 1329–1343. Dec. https://doi.org/10.1243/09544119JEIM770.

Bukara, K., et al., 2016. Ordered mesoporous silica to enhance the bioavailability of poorly water-soluble drugs: Proof of concept in man. Eur. J. Pharm. Biopharm. 108 https://doi.org/10.1016/j.ejpb.2016.08.020. Sep.

Carmel, B., 2012. In: Queensberry, K.E., Carpenter, J.W. (Eds.), Ferrets, rabbits and rodents: clinical medicine and surgery, 3rd edn. Elsevier, St Louis, p. 596. Price $81.99. ISBN 978 1 41606 621 7.', Aust Vet J, vol. 90, Nov. 2012. https://doi.org/10.1111/j.1751-0813.2012.00987.x.

Chai, Q., Jiao, Y., Yu, X., Jan. 2017. Hydrogels for Biomedical applications: their Characteristics and the Mechanisms behind Them. Gels 3, 6. https://doi.org/10.3390/gels3010006.

Costa, P., 2001. An alternative method to the evaluation of similarity factor in dissolution testing. Int. J. Pharm. 220 (1), 77–83. https://doi.org/10.1016/S0378-5173(01)00651-2.

Danaei, M., et al., 2018. Impact of Particle Size and Polydispersity Index on the Clinical Applications of Lipidic Nanocarrier Systems. Pharmaceutics 10 (2). https://doi.org/10.3390/pharmaceutics10020057.

Donatti, D.A., Ruiz, A.I., Vollet, D.R., 2002. A dissolution and reaction modeling for hydrolysis of TEOS in heterogeneous TEOS–water–HCl mixtures under ultrasound stimulation. Ultrason. Sonochem. 9 (3), 133–138. https://doi.org/10.1016/S1350-4177(01)00120-1.

Eldeeb, A.E., Salah, S., Amer, M.S., Elkasabgy, N.A., 2022a. 3D nanocomposite alginate hydrogel loaded with pitavastatin nanovesicles as a functional wound dressing with controlled drug release; preparation, in-vitro and in-vivo evaluation. J. Drug Deliv. Sci. Technol. 71, 103292. https://doi.org/10.1016/j.jddst.2022.103292.

Eldeeb, A.E., Salah, S., Mabrouk, M., Amer, M.S., Elkasabgy, N.A., 2022b. Dual-Drug Delivery via Zein In Situ Forming Implants Augmented with Titanium-Doped Bioactive Glass for Bone Regeneration: Preparation, In Vitro Characterization, and In Vivo Evaluation. Pharmaceutics 14 (2). https://doi.org/10.3390/pharmaceutics14020274.

Elkasabgy, N.A., Mahmoud, A.A., Shamma, R.N., 2018. Determination of cytocompatibility and osteogenesis properties of in situ forming collagen-based scaffolds loaded with bone synthesizing drug for bone tissue engineering. Int. J. Polym. Mater. Polym. Biomater. 67 (8), 494–500. May. https://doi.org/10.1080/00914037.2017.1354195.

Florczyk, S.J., et al., Dec. 2012. Enhanced bone tissue formation by alginate gel-assisted cell seeding in porous ceramic scaffolds and sustained release of growth factor. J. Biomed. Mater. Res. A 100A (12), 3408–3415. https://doi.org/10.1002/jbm.a.34288.

González, R., Peña, M.Á., Torres, N.S., Torrado, G., 2022. Design, development, and characterization of amorphous rosuvastatin calcium tablets. PLoS One 17 (3), e0265263 [Online]. Available. Mar. https://doi.org/10.1371/journal.pone.0265263.

Janjua, T.I., Cao, Y., Yu, C., Popat, A., 2021. Clinical translation of silica nanoparticles. Nat. Rev. Mater. 6 (12), 1072–1074. https://doi.org/10.1038/s41578-021-00385-x.

Li, Z., Mu, Y., Peng, C., Lavin, M.F., Shao, H., Du, Z., 2021. Understanding the mechanisms of silica nanoparticles for nanomedicine. WIREs Nanomed. Nanobiotechnol. 13 (1), e1658. Jan. https://doi.org/10.1002/wnan.1658.

Lu, Z., Owens, H., 2018. A method to improve the quality of silica nanoparticles (SNPs) over increasing storage durations. J. Nanopart. Res. 20 (8), 213. https://doi.org/10.1007/s11051-018-4282-7.

Luvai, A., Mbagaya, W., Hall, A., Barth, J., Feb. 2012. Rosuvastatin: a Review of the Pharmacology and Clinical Effectiveness in Cardiovascular Disease. Clin. Med. Insights Cardiol. 6, 17–33. https://doi.org/10.4137/CMC.S4324.

Maged, A., Abdelkhalek, A., Mahmoud, A., Salah, S., Ammar, M., Ghorab, M., 2018. Mesenchymal stem cells associated with chitosan scaffolds loaded with rosuvastatin to improve wound healing. Eur. J. Pharm. Sci. 127 https://doi.org/10.1016/j.ejps.2018.11.002. Nov.

Meola, T., Abuhelwa, A., Joyce, P., Clifton, P., Prestidge, C., 2020. A safety, tolerability, and pharmacokinetic study of a novel simvastatin silica-lipid hybrid formulation in healthy male participants'. Drug Deliv. Transl. Res. 11 https://doi.org/10.1007/s13346-020-00853-x. Sep.

Mohammed, M.A., Syeda, J.T.M., Wasan, K.M., Wasan, E.K., 2017. An Overview of Chitosan Nanoparticles and Its Application in Non-Parenteral Drug Delivery. Pharmaceutics 9 (4). https://doi.org/10.3390/pharmaceutics9040053.

Mohseni, M., Gilani, K., Mortazavi, S., Dec. 2015. Preparation and Characterization of Rifampin Loaded Mesoporous Silica Nanoparticles as a potential System for Pulmonary Drug delivery. Iran J. Pharm. Res. 14, 27–34.

Nan, N.F.C., Zainuddin, N., Ahmad, M., Jan. 2019. Preparation and swelling study of CMC hydrogel as potential superabsorbent. Pertanika J. Sci. Technol. 27, 489–498.

Padma, G.T., Rao, T.S., Naidu, K.C.B., 2018. Preparation, characterization and dielectric properties of sodium alginate/titanium dioxide composite membranes. SN Appl. Sci. 1 (1), 75. https://doi.org/10.1007/s42452-018-0083-y.

Panwar, K., Jassal, M., Agrawal, A.K., 2015. In situ synthesis of Ag–SiO2 Janus particles with epoxy functionality for textile applications. Particuology 19, 107–112. https://doi.org/10.1016/j.partic.2014.06.007.

Porrang, S., Davaran, S., Allahyari, S., Allahyari, S., Mostafavi, E., 2022. How advancing are Mesoporous Silica Nanoparticles? A Comprehensive Review of the Literature. Int. J. Nanomedicine 17, 1803–1827. Apr. https://doi.org/10.2147/IJN.S353349.

Rao, K.M., Mallikarjuna, B., Rao, K.S.V. Krishna, Sudhakar, K., Rao, K.C., Subha, M.C.S., 2013. Synthesis and Characterization of pH Sensitive Poly (Hydroxy Ethyl Methacrylate-co-acrylamidoglycolic Acid) based Hydrogels for Controlled Release Studies of 5-Fluorouracil. Int. J. Polym. Mater. Polym. Biomater. 62 (11), 565–571. May. https://doi.org/10.1080/00914037.2013.769160.

Rhimi, A., Zlaoui, K., Horchani-Naifer, K., Ennigrou, D.J., 2022. Characterization and extraction of sodium alginate from Tunisian algae: synthesizing a cross-linked

ultrafiltration membrane. Iran. Polym. J. 31 (3), 367–382. https://doi.org/10.1007/s13726-021-01005-9.
Rubert, M., Alonso-Sande, M., Monjo, M., Ramis, J.M., 2012. Evaluation of alginate and hyaluronic acid for their use in bone tissue engineering. Biointerphases 7 (1), 44. https://doi.org/10.1007/s13758-012-0044-8.
Rubio, F., Rubio, J., Oteo, J.L., 1998. A FT-IR Study of the Hydrolysis of Tetraethylorthosilicate (TEOS). Spectrosc. Lett. 31 (1), 199–219. Jan. https://doi.org/10.1080/00387019808006772.
Safari, B., Aghanejad, A., Roshangar, L., Davaran, S., 2020. Osteogenic effects of the bioactive small molecules and minerals in the scaffold-based bone tissue engineering. Colloids Surf. B: Biointerfaces 198, 111462. Nov. https://doi.org/10.1016/j.colsurfb.2020.111462.
Sahoo, D.R., Biswal, T., 2021. Alginate and its application to tissue engineering. SN Appl. Sci. 3 (1), 30. https://doi.org/10.1007/s42452-020-04096-w.
Sarfraz, R.M., Ahmad, M., Mahmood, A., Minhas, M.U., Yaqoob, A., Dec. 2017. Development and Evaluation of Rosuvastatin Calcium based Microparticles for Solubility Enhancement: an in Vitro Study. Adv. Polym. Technol. 36 (4), 433–441. https://doi.org/10.1002/adv.21625.
Selvarajan, V., Obuobi, S., Ee, P.L.R., 2020. Silica Nanoparticles—A versatile tool for the treatment of bacterial infections. Front. Chem. 8 https://doi.org/10.3389/fchem.2020.00602.
Shiralashetti, S., Shivanand, S., Patil, J., 2014. Characterization and evaluation of inclusion complexes of poorly soluble rosuvastatin calcium. Univ. J. Pharm. Design 2014. Apr.
Stöber, W., Fink, A., Bohn, E., 1968. Controlled growth of monodisperse silica spheres in the micron size range. J. Colloid Interface Sci. 26 (1), 62–69. https://doi.org/10.1016/0021-9797(68)90272-5.
T. A and A. MS, 2016. Synthetic Characterization of Complexes of Rosuvastatin and Some ACE Inhibitors: Pharmacological Evaluation. Pharm. Anal. Acta 7. https://doi.org/10.4172/2153-2435.1000488. Jan.
Tan, A., Eskandar, N.G., Rao, S., Prestidge, C.A., 2014. First in man bioavailability and tolerability studies of a silica–lipid hybrid (Lipoceramic) formulation: a phase I study with ibuprofen. Drug Deliv. Transl. Res. 4 (3), 212–221. https://doi.org/10.1007/s13346-013-0172-9.
Tawfik, M.A., Eltaweel, M.M., Fatouh, A.M., Shamsel-Din, H.A., Ibrahim, A.B., 2023. Brain targeting of zolmitriptan via transdermal terpesomes: statistical optimization and in vivo biodistribution study by 99mTc radiolabeling technique. Drug Deliv. Transl. Res. https://doi.org/10.1007/s13346-023-01373-0.
Varma, R., Vasudevan, S., Aug. 2020. Extraction, Characterization, and Antimicrobial activity of Chitosan from Horse Mussel Modiolus modiolus. ACS Omega 5 (32), 20224–20230. https://doi.org/10.1021/acsomega.0c01903.
Venkatesan, J., Bhatnagar, I., Manivasagan, P., Kang, K.-H., Kim, S.-K., 2015. Alginate composites for bone tissue engineering: a review. Int. J. Biol. Macromol. 72, 269–281. https://doi.org/10.1016/j.ijbiomac.2014.07.008.
Young, S., et al., Jul. 2008. Development and characterization of a rabbit alveolar bone nonhealing defect model. J. Biomed. Mater. Res. A 86A (1), 182–194. https://doi.org/10.1002/jbm.a.31639.
Zaghloul, N., El Hoffy, N.M., Mahmoud, A.A., Elkasabgy, N.A., 2022. Cyclodextrin Stabilized Freeze-Dried Silica/Chitosan Nanoparticles for Improved Terconazole Ocular Bioavailability. Pharmaceutics 14 (3). https://doi.org/10.3390/pharmaceutics14030470.
Zhao, L., et al., 2021. Effects of Different Drying Methods on the Characterization, Dissolution Rate and Antioxidant Activity of Ursolic Acid-Loaded Chitosan Nanoparticles. Foods 10 (10). https://doi.org/10.3390/foods10102470.